THE JOURNAL OF PHYSICAL CHEMISTRY C
A JOURNAL OF THE AMERICAN CHEMICAL SOCIETY

pubs.acs.org/JPCC

Article

Interaction of Hydrogen with Cu-Modified Cerium Oxide Surfaces

Avinash Vikatakavi, Stefania Benedetti, Giulia Righi, Rita Magri, Sergio D'Addato, Paola Luches,* and Annabella Selloni

Cite This: *J. Phys. Chem. C* 2022, 126, 18652−18660

Read Online

ACCESS | Metrics & More | Article Recommendations | Supporting Information

ABSTRACT: We investigate the interaction between molecular hydrogen and ultrathin epitaxial CeO_2 films modified with a 2% concentration of Cu atoms using X-ray photoemission spectroscopy (XPS) during thermal reduction cycles in H_2. The XPS measurements are combined with density functional theory calculations to obtain further insight into the observed modifications of the film surface. Our results show that the presence of Cu atoms decreases the barrier for H_2 dissociation in comparison to that on pure ceria surfaces, leading to the formation of surface OH groups after exposure to H_2. Moreover, surface oxygen vacancies are generated already at mild temperatures (470 K), most likely via water formation and desorption. The presence of surface oxygen vacancies and hydroxyls contributes to the observed large increase in surface Ce^{3+} concentration with increasing reduction temperature. In spite of these atomic scale modifications, the surface morphology observed by scanning tunneling microscopy remains substantially unchanged on the length scale of tens of nm.

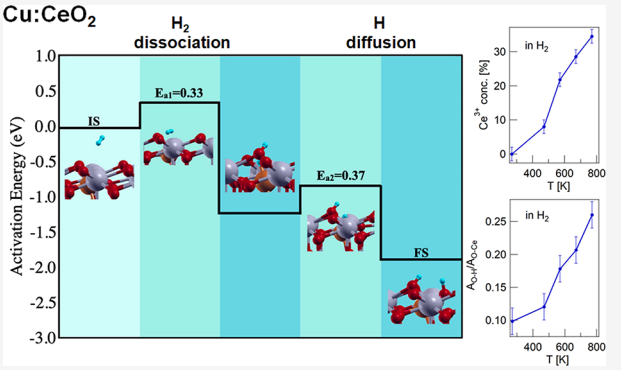

INTRODUCTION

The growing importance of hydrogen in various technological applications has generated significant interest in a detailed atomic scale characterization of the underlying processes of hydrogen adsorption, dissociation, and desorption on different solid surfaces. The resulting understanding can also help the rational design of catalysts for hydrogen synthesis and is important in the context of hydrogenation reactions and fuel cells.[2−4]

Efficient catalysts for hydrogen dissociation are typically based on rare and expensive materials, like platinum-group metal nanoparticles.[5−7] To overcome this limitation, intensive research efforts have focused on the identification and synthesis of more abundant materials, capable of partially substituting precious metals in hydrogen-based applications.[2−4,7−9] Oxides are often used as supports for metal catalysts to prevent nanoparticle sintering and promote their activity. Oxides have also been shown to take an active part in many reactions, allowing a substantial decrease in noble metal concentration within the catalyst.[10,11]

Among catalytically active oxides, cerium oxide is of special interest for its reducibility, i.e., the easy formation and diffusion of oxygen vacancies. This property is related to the comparable stability of Ce^{4+} and Ce^{3+} ions under different conditions due to the presence of Ce 4f levels that can easily accept or donate electrons close to the Fermi level.[12] Moreover, the modification of cerium oxide with a low concentration of aliovalent metals has been shown to induce significant modifications of the properties of the material.[10,13−16] Cerium oxide has been widely investigated for hydrogenation reactions,[3,17−19] and many studies have examined the detailed mechanisms of its interaction with molecular hydrogen. Early experimental work was done on powdered catalysts by temperature-programmed reduction (TPR) in H_2. The TPR spectra showed two main peaks at 770 and 1100 K, which were initially assigned to the release of surface and bulk oxygen, respectively.[20] The modification of ceria with metals was shown to decrease the onset of surface reduction,[21] but in powdered catalysts, many different variables like particle size and exposed facet can affect the behavior of the material, complicating the interpretation of TPR results.[22,23]

Studies of model systems in the form of bulk or well-controlled ultrathin film surfaces in combination with density functional theory (DFT)-based modeling can provide important insights into the interactions that take place at the atomic scale. In particular, DFT studies have shown that H_2 dissociation on the most stable CeO_2 (111) surface has a barrier of approximately 1 eV, independent of the presence of O surface vacancies.[24] Moreover, simulations based on *ab initio* molecular dynamics showed that thermal effects can significantly affect the mechanisms for H_2 dissociation.[25]

Received: June 27, 2022
Revised: October 14, 2022
Published: October 28, 2022

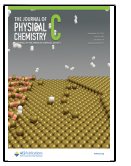

Experimental investigations reported that dissociated H_2 is localized on the surface in the form of OH groups, while the presence of O vacancies helps the migration of H species to the subsurface region.[26] On the Pt:CeO_2 system, H_2 dissociation was demonstrated to be very efficient and to take place on highly dispersed metallic Pt species.[27] Similarly, Ag:CeO_2 was found to have a higher reactivity toward H_2 oxidation than pure CeO_2 due to a decreased barrier for H_2 dissociative adsorption and diffusion.[1] By exposing stoichiometric and partially reduced CeO_2(111) thin films to atomic hydrogen, Chen et al. showed that the stability of OH was enhanced by the presence of surface oxygen vacancies.[28] Copper atoms have also been used to dope cerium oxide. The Cu ions were shown to occupy cerium substitutional sites and to enhance the reducibility due to the lower valence of Cu compared to Ce.[15,29,30]

In a previous work, we have demonstrated that ultrathin Cu- and Ag-doped cerium oxide nanostructures supported on Pt(111) have a higher reducibility than pure CeO_2 nanostructures when annealed in vacuum.[15] To investigate the interaction of H_2 with pure and Ag-doped ceria, we have used epitaxial films, with a higher thickness than the nanostructures studied in ref 15, to avoid any effect from the Pt(111) support.[1] An important result obtained is that the Ag dopants play an active role by capturing part of the charge released by oxygen vacancy formation or hydrogen dissociation.[1] In this work, we investigate the behavior of an epitaxial film of Cu-modified cerium oxide during reducing cycles in vacuum and in hydrogen. With the help of DFT theoretical modeling, we determine the atomic scale details that underlie the reactivity toward hydrogen dissociation. The results of this work provide insight into the interaction between modified oxides and hydrogen molecules and could help optimize the functionality of these materials for future hydrogen-based applications. In particular, a remarkably different behavior of Cu as compared to Ag dopants is highlighted, with the presence of Cu^{1+} species significantly enhancing the material reactivity.

METHODS

Experimental Methods. The sample used for the present study was grown in an ultrahigh vacuum (UHV) apparatus, equipped with facilities for surface preparation, for molecular beam epitaxy (MBE) growth, and for X-ray photoemission spectroscopy (XPS) and scanning tunneling microscopy (STM) characterization. The experimental chamber was also provided with two gas lines for O_2 and H_2 exposure. The lines were pumped before each experiment, and the purity of the gases was checked using a residual gas analyzer present in the experimental chamber to exclude in particular any contamination by H_2O. The substrate was a Pt(111) single crystal, previously shown to favor the growth of (111)-oriented epitaxial CeO_2 films.[31,32] The substrate was prepared by repeated cycles of Ar^+ ion sputtering (1 keV, 1 $\mu A/cm^2$) and thermal annealing (1040 K). The Cu-modified cerium oxide (Cu:CeO_2) film was obtained by reactive MBE by simultaneously growing Ce and Cu in O_2 partial pressure ($P_{O2} = 10^{-7}$ mbar) on the substrate kept at room temperature (RT). An e-beam cell was used for Ce evaporation, while an effusion cell was used for Cu. The evaporation rates of Ce and Cu were calibrated via a quartz crystal microbalance to obtain a nominal Cu atomic concentration of 3%. The film thickness was chosen to be 5.7 ML to completely cover the substrate surface, in analogy with the pure CeO_2 and Ag:CeO_2 films investigated in ref 1. After the growth, the films were annealed in O_2 partial pressure ($P_{O2} = 10^{-7}$ mbar) at 770 K for 45 min to improve surface morphology, stoichiometry, and structure. Reducing thermal treatments in UHV and in H_2 partial pressure ($P_{H2} = 10^{-7}$ mbar) were performed using an electron bombardment heater. The sample was subsequently heated at a constant rate (60 K/min), kept at the set temperature (470, 570, 670, and 770 K) for 15 min, and cooled to RT, first in UHV and—after reoxidation ($P_{O2} = 10^{-7}$ mbar, 770 K, 15 min)—in H_2. During the cooling stages after the thermal treatments in H_2 and in O_2, the gas lines were closed when the sample reached a temperature lower than 370 K.

After growth, after reoxidation, and after each reduction step in UHV and in H_2, XPS was used to measure the sample surface composition. The XPS measurements were always acquired at RT after each step of the reducing thermal treatment. For the purpose, we used an Al Kα X-ray source and a hemispherical electron analyzer at grazing emission geometry (65° from sample normal) to increase surface sensitivity. The Ce 3d, O 1s, Pt $4p_{3/2}$, Pt 4f, and Cu 2p spectra were measured using a pass energy PE = 30 eV. XPS data processing consisted in subtracting a Shirley-type background and fitting with Voigt-shaped peaks. The Ce 3d spectra were fit using five doublets, following the procedure introduced by Skála et al.,[33] to obtain the Ce^{3+} concentration as the ratio of the area of the two Ce^{3+}-related doublets with respect to the total Ce 3d area. The only free fitting parameters were the intensity of the peaks and a single rigid shift of the binding energies of all the components, for which the energy separation is kept fixed. An example of one of the Ce 3d spectra and the fitting components are shown in the Supporting Information, Figure S1. The fit allows one to obtain rather precise evaluations of Ce^{3+} concentration, while the accuracy of the obtained numbers is affected by a systematic error, which originates from background subtraction, and from a higher complexity of the spectra as compared to the simplified fitting model used here.[34] However, the approximations used do not affect the considerations exposed in this work, which are based on the variation of Ce^{3+} concentration with the different treatments, rather than on its absolute value. The O 1s spectra were fit using two peaks, one related to lattice oxygen and a second one, at approximately 2 eV higher binding energy, related to OH groups on the surface. In the O 1s fitting procedure, the binding energy and width of the main peak were fixed, leaving only the peak intensity as a free fitting parameter, while for the OH-related peak, also the binding energy was allowed for moderate changes to optimize the fit. The Pt $4p_{3/2}$ peak was fit as a single peak, with variable intensity and binding energy and fixed width. An example of an XPS spectrum with the O 1s and Pt 4p3/2 peaks and the fitting components are shown in the Supporting Information, Figure S2. The peak positions and intensities obtained from the fits of all the XPS spectra are reported in the Supporting Information (Tables S1 and S2). The Pt 4f levels were used to calibrate the binding energy scale of the spectra, while the Cu 2p intensity was used to estimate the Cu doping concentration (see the Supporting Information, Figure S3). The errors on the intensities of the XPS lines were derived from the fitting procedure and used to obtain the error bars on the intensity ratios shown in the figures.

RT STM was used to measure the surface topography of the sample before and after the thermal treatments using a W tip

https://doi.org/10.1021/acs.jpcc.2c04442
J. Phys. Chem. C 2022, 126, 18652−18660

working in constant current mode at a positive sample-to-tip bias. WSxM software was used for image processing.[35]

Low-energy electron diffraction patterns of the surface before and after the full reducing treatment in H_2 are shown in the Supporting Information (Figure S4).

Theoretical Methods. The structural and electronic properties of Cu-doped CeO_2 were investigated via density functional theory (DFT) calculations performed with the Quantum Espresso Package.[36,37] We used ultrasoft pseudopotentials to describe the interaction of Ce, Ag, Cu, and O ions with the valence electrons and the functional of Perdew, Burke, and Ernzerhof (PBE) for the exchange−correlation potential.[38] To account for the localized and strongly correlated character of the Ce 4f electrons, we used the Hubbard correction (DFT + U) as implemented by Cococcioni and de Gironcoli.[39] We adopted U = 4 eV, a value that well reproduces the experimental results.[30]

The CeO_2 (111) surface was described using slabs with three O−Ce−O trilayers and a (4 × 4) surface supercell. The vacuum layers separating the slabs are 15 Å thick. The Brillouin zone was sampled only at the Γ point. The positions of the atoms of two trilayers were optimized with convergence thresholds of 1×10^{-5} eV and 1×10^{-2} eV/Å for the total energy and ionic forces, respectively, while those of the last trilayer were kept fixed to simulate the bulk constraint.

To model the Cu-modified surface, we considered a Cu atom substituting one of the Ce atoms of the first trilayer.

It was indeed found that noble metals prefer to substitute Ce atoms rather than being inserted in interstitial positions or substituting O atoms.[40,41] The Cu dopant was compensated with an oxygen vacancy, which was indeed found to have a negative formation energy (−0.12 eV).[30]

We calculated the oxygen vacancy formation energy of the Cu-doped slab as:

$$E_{\text{form}} = E_{\text{Cu:CeO}_{2-x}} - E_{\text{Cu:CeO}_{2-y}} + \frac{1}{2}E_{\text{O}_2}$$

where $E_{\text{Cu : CeO}_{2-x}}$ and $E_{\text{Cu : CeO}_{2-y}}$ are the energies of the slabs of reduced ceria with a single copper atom, x corresponds to one more oxygen vacancy than y, and E_{O_2} is the energy of the oxygen molecule (from calculations with a single O_2 inside a cubic box of 15 Å edge).

To determine the minimum energy paths (MEPs) of H_2 dissociation on the Cu:CeO_2 surfaces, we used the climbing image nudged elastic band method (CI-NEB)[42] with seven images.

Charge transfers and ion oxidation states were estimated using the Bader approach[43] and by the analysis of the partial densities of states.

RESULTS

Experimental Results. The analysis of the Ce 3d XPS spectra allowed us to determine the evolution of the Ce^{3+} concentration on the film surface during the reduction cycles. As shown in Figure 1a, before the thermal treatment, the spectrum has the characteristic shape of compounds containing only Ce^{4+} ions. This means that the introduction of Cu atoms in 3% concentration within a CeO_2 film does not induce detectable deviations of the Ce oxidation state, the Ce^{3+} concentration being below the detection limit. The thermal treatments in UHV induce only minor modifications of the shape of the Ce 3d spectra (red line in Figure 1a). The

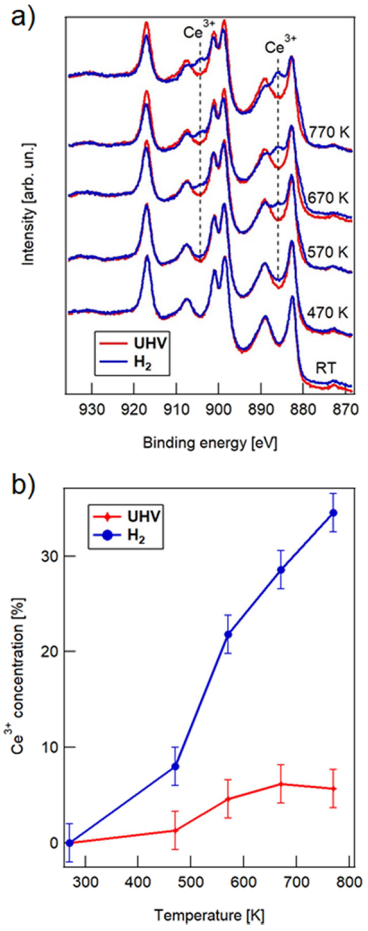

Figure 1. (a) Ce 3d XPS spectra of the Cu:CeO_2 sample measured at RT after the different thermal annealing steps in UHV (red curves) and in H_2 (blue curves). (b) Evolution of the Ce^{3+} concentration, evaluated from the fitting of the Ce 3d spectra, with temperature in UHV (red diamonds) and in H_2 (blue dots).

introduction of H_2 at RT is also not effective in modifying the sample surface stoichiometry. On the contrary, the thermal treatments in H_2 induce significant modifications of the spectra, consistent with the reduction of a non-negligible fraction of Ce ions (blue line in Figure 1a). The evolution of Ce^{3+} concentration with temperature, estimated from the fitting of the Ce 3d spectra (see also the Supporting Information, Figure S1), is shown in Figure 1b. In UHV, the Ce^{3+} concentration increases mildly with temperature, reaching approximately 5%, while it shows a very rapid increase, up to 35% at 770 K, in H_2.

To gain information on the possible presence of adsorbed OH or water surface species during the reducing treatments, the O 1s XPS spectra after each thermal step in UHV and in H_2 were also measured (Figure 2a). The O 1s spectra of the as-grown Cu:CeO_2 sample show a slightly asymmetric shape toward higher binding energy even before the introduction of H_2 at RT. Some remarks can be made on the origin of the asymmetry. The O 1s binding energy in ceria is known to be very slightly shifted in the presence of O vacancies or O atoms with reduced coordination.[44] However, terrace steps and defects, which have a non-negligible density on the surface of the samples we investigated (see below), were shown to be more effective dissociation sites as compared to regular (111) surface sites.[45] Therefore, a possible reason for the asymmetry

https://doi.org/10.1021/acs.jpcc.2c04442
J. Phys. Chem. C 2022, 126, 18652−18660

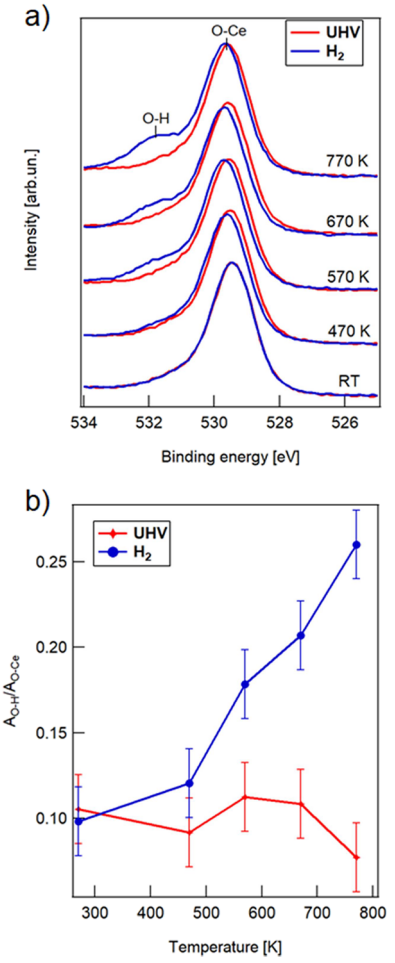

Figure 2. (a) O 1s XPS spectra of the Cu:CeO_2 sample measured at RT after the different thermal annealing steps in UHV (red curves) and in H_2 (blue curves). (b) Ratio between the areas of the two peaks corresponding to OH and to lattice oxygen, evaluated from the fitting of the O 1s spectra, at each thermal annealing step in UHV (red diamonds) and in H_2 (blue dots).

is the presence of some OH species on the surface even before any treatment in H_2 due to the dissociative adsorption at defect sites of H_2 and/or H_2O molecules present in the residual pressure of the UHV chamber. The possibility that the high binding energy shoulder is due to O atoms coordinated to Cu is ruled out, since its binding energy is not compatible with the one expected for Cu−O bonds,[46] even though the large structural distortions expected to be induced by Cu[47] may represent further dissociation sites. The presence of C−O bonds on the surface, expected to induce a 2 eV binding energy shift in O 1s peaks, can be excluded, since the C 1s signal intensity on the film surface was below the sensitivity of XPS. While the thermal treatment in UHV does not induce relevant modifications of the O 1s line shape (red curves in Figure 2a), the treatment in H_2 induces the progressive formation of a marked shoulder at ∼2 eV higher binding energy (blue curves in Figure 2a), which is ascribed to the formation of O−H bonds on the surface. The results of the fitting of the O 1s spectra shown in Figure 2b provide information on the relative intensity of the peaks related to O−H bonds and to lattice oxygen (see also the Supporting Information, Figure S2a). As shown in Figure 2b, the weight of the OH peak does not change significantly during the reducing cycle in UHV, while it increases with temperature in H_2, reaching approximately 25% at 770 K. Moreover, the results of the fit also show that the binding energy of the shoulder peak progressively shifts toward higher binding energies with increasing temperature in H_2, the binding energy separation from the O 1s main peak being 1.65 eV at RT and 2.0 eV at 770 K in H_2 (see the Supporting Information, Figure S2b). This supports the hypothesis that the initial asymmetry is due to OH groups mainly present at defect sites, while, with H_2 exposure at increasing temperature, OH groups also form at regular surface sites. We note that the O 1s spectra do not show any peak ascribable to the presence of adsorbed water on the surface, which is expected at approximately 5 eV higher binding energy with respect to the lattice oxygen-related peak[48] (see the Supporting Information, Figure S2a).

Since the O 1s and Pt $4p_{3/2}$ photoelectrons have very close kinetic energies (see the Supporting Information, Figure S2a) and consequently comparable escape depths, the ratio of the intensity of the two peaks was used to determine the evolution of oxygen vacancy concentration with the different treatments. Figure 3 reports the ratio between the O−Ce, e O−H and total O 1s intensity and the Pt $4p_{3/2}$ intensity and their evolution with the thermal treatments in UHV and in H_2. The two components in Figure 3a,b do not show relevant variations in UHV, consistent with the very small increase in Ce^{3+} concentration observed in Figure 1b (we note that O 1s photoelectrons have a lower surface sensitivity than Ce 3d ones due to their higher kinetic energy and, therefore, the O 1s intensity is less sensitive to small changes in surface stoichiometry than Ce 3d). In H_2, the O−Ce component drops significantly after the treatment at 470 K, while for higher temperatures, its decrease is less pronounced (Figure 3a). The increase in OH intensity is instead mild at 470 K and more pronounced at higher temperatures (Figure 3b). The observed trend may indicate that a process that leads to the formation of O vacancies in H_2, namely, water formation and desorption, is initiated at 470 K, possibly inducing the removal of O atoms with low coordination from defect sites. At higher temperatures, the O−Ce decrease is less pronounced, possibly due to the finite density of defect sites and the need of temperatures even higher than 770 K to remove further O atoms from regular surface sites. This explains the trend of the total O signal (Figure 3c), which is systematically lower in H_2 than in UHV (despite the large error bars due to the low intensity of the Pt $4p_{3/2}$ signal), with the drop at 470 K indicating the onset of water formation and the essentially constant trend at higher temperatures being due to further water formation and desorption, partially compensated by the readsorption of OH species during the cooling phase.

The Cu 2p line shape has a rather low intensity, and it is superimposed with a plasmon-related satellite of Ce 3d line. The Cu LMM Auger line, often used for the identification of the Cu oxidation state, has an even lower intensity. In spite of the relatively long acquisition times, it was not possible to unambiguously determine the Cu oxidation state and its possible evolution from the spectra (see the Supporting Information, Figure S3).

The morphology of the sample surface was investigated by STM. Figure 4 shows the surface topography before the full reducing thermal treatment in H_2. The surface morphology is rather rough and shows different contrast levels. The brighter contrast areas are irregular protrusions with a lateral size below 10 nm. The surface below the protrusions is not uniform. The

https://doi.org/10.1021/acs.jpcc.2c04442
J. Phys. Chem. C 2022, 126, 18652−18660

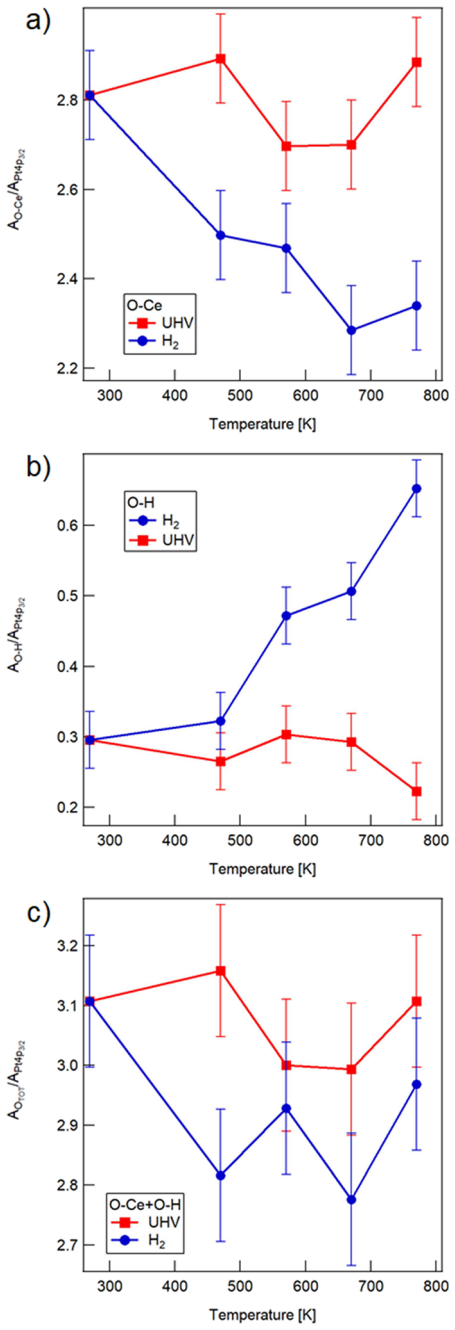

Figure 3. Ratio between the area of the different components of O 1s and the area of Pt $4p_{3/2}$ XPS peaks for the $Cu:CeO_2$ sample measured at RT after the different thermal annealing steps in UHV (red squares) and in H_2 (blue dots): (a) O−Ce component; (b) O−H component; (c) sum of the two components.

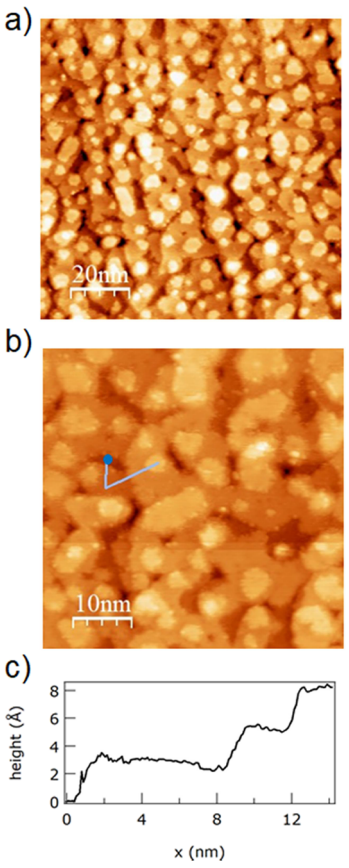

Figure 4. STM images of the $Cu:CeO_2$ sample: (a) 100 × 100 nm^2 (2.7 V, 0.03 nA); (b) 50 × 50 nm^2 (2.67 V, 0.03 nA). (c) Height profile across the blue broken line shown in panel (b). The blue dot marks the initial point of the profile.

height difference between the different contrast levels, as shown by the height profile in Figure 4c, is compatible with different $CeO_2(111)$ planes being exposed (expected interplanar distance, 3.12 Å). After the reducing treatments in H_2, STM imaging was unstable, possibly due to the interaction between the tip and OH groups on the surface. However, major morphological rearrangements could be excluded (see the Supporting Information, Figure S5).

Theoretical Results. To gain insight into the evolution of the Ce^{3+} ion concentration during the thermal cycles, we studied the reduction of the $Cu:CeO_2$ surface using DFT. In our calculations, the stable $Cu:CeO_2$ surface has a compensating oxygen vacancy, V_o, located near the Cu atom, which has a 2+ oxidation state (Cu^{2+}).

Reduction in Vacuum. The increase in temperature can lead to the formation of additional oxygen vacancies on the stable surface. To investigate this possibility, we considered the formation of a second V_o (additional to the charge compensating one). Two kinds of oxygen vacancies can be created on the stable surface. In the first one, with E_{form} = 1.0 eV, the removed O is not one of the four oxygens directly bonded to the Cu atom, but one of the atoms displaced away from it by the Cu-induced distortion of the CeO_2 lattice. Since the removed oxygen does not form a direct bond with Cu, the oxidation state of the noble metal remains the same, Cu^{2+}, whereas two Ce ions are reduced to Ce^{3+}. In the other type of vacancy, with E_{form} = 1.4 eV, the removal of an oxygen atom bonded to Cu leads to the reduction of Cu^{2+} to Cu^{1+} and the delocalization of some additional negative charge on two Ce ions and on surface O ions. For comparison, the oxygen vacancy formation energy is much higher, E_{form} = 2.02 eV, on the pristine ceria surface. Thus, the thermal treatment creates more oxygen vacancies at lower temperatures on the Cu-modified surface than on pristine ceria and some of these V_o's will produce Cu^{1+} species. These are highly reactive, since the preferred oxidation state of Cu is Cu^{2+}.

Reduction in a H_2 Atmosphere. In a H_2 atmosphere, an additional reaction, H_2 dissociative adsorption, can occur. This reaction, like the creation of oxygen vacancies, is activated by

https://doi.org/10.1021/acs.jpcc.2c04442
J. Phys. Chem. C 2022, 126, 18652−18660

the increase in temperature. On the stable Cu:CeO_2 surface, the activation energy E_a for H_2 dissociation is slightly smaller than on pristine ceria (+0.80 eV against 0.99 eV). However, the presence of the highly reactive Cu^{1+} species on the surface can decrease the energy barrier for H_2 dissociation substantially. To show this, we have considered the stable surface with one additional V_o per unit cell generating the Cu^{1+} cation and obtained a strongly decreased E_{a1} = 0.33 eV for the H_2 dissociation barrier. In Figure 5, the calculated minimum energy path (MEP) for H_2 dissociation on such a surface is shown.

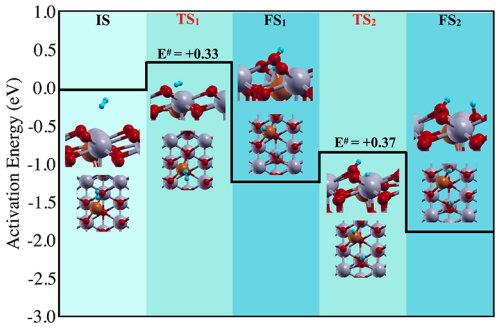

Figure 5. Minimum energy path (MEP) for H_2 dissociation on the Cu:CeO_{2-x} surface with two (one compensating and one additional) O vacancies and the Cu^{1+} cation at T = 0 K. IS denotes the initial state, and TS_1 and TS_2 denote the transition states whose activation energies (in eV) are 0.33 and 0.37, respectively. FS_1 is the first final state after H_2 dissociation with one H on the Cu atom, and FS_2 is the second final state at a lower energy with the H atoms on two O atoms. In the side and top views shown for each state, gray, red, and orange balls represent Ce, O, and Cu atoms, respectively, while the small light-blue balls are H atoms.

The Cu^{1+} cation plays an active role in the dissociation of the H_2 molecule, at variance with what occurs with the Cu^{2+} cation. H_2 binds first to Cu and to an O atom, lowering the activation barrier and facilitating the breaking of the molecule. The 0.33 eV activation barrier in the presence of Cu^{1+} is similar to the one calculated for Ag:CeO_2.[30]

In the last step, the hydrogen atom moves to a nearby oxygen atom, overcoming a similar energy barrier, 0.37 eV, to complete the dissociative adsorption of hydrogen on the surface, which gives rise to two O−H groups. Altogether, our DFT calculations suggest that a larger number of oxygen vacancies are formed on the Cu:CeO_2 surface than on pristine ceria with increasing temperature. Although most of these vacancies generate Ce^{3+} cations, Cu^{1+} cations are also generated. These species favor the low-temperature dissociation of the H_2 molecules and the consequent formation of OH groups on the surface. The adsorbed hydrogen atoms donate electrons to the surface, increasing the Ce^{3+} and Cu^{1+} surface concentration. The higher the temperature, the higher is the expected concentration of Cu^{1+} cations and the consequential increase in the dissociative H_2 adsorption on the surface.

We note that the supercell size does not significantly influence the computed formation energy of the first (compensating) oxygen vacancy, which has a comparable value in the case of (3 × 3) and (4 × 4) unit cells, as considered here. By analogy, we do not expect a significant dependence of the activation barriers on the size of the supercell used for the calculations.

DISCUSSION

Our combined experimental and DTF results allow us to obtain valuable information on the interaction between Cu:CeO_2 and H_2. Our calculations predict a barrier for H_2 dissociation on the stable (111) surface of Cu:CeO_{2-x} of 0.8 eV, not significantly lower than the barrier on the pure CeO_2 surface (0.99 eV).[1,30] However, the dissociative adsorption of H_2 on Cu:CeO_{2-x} leads to the reduction of a Ce ion from 4+ to 3+ and of a Cu ion from 2+ to 1+. The Cu^{1+} species is very reactive and significantly decreases the dissociation barrier for an additional H_2 to about 0.33 eV, a value much lower than on pure CeO_2.[1,30] Based on these results, it is reasonable to assume that the initial dissociation of H_2 on the Cu:CeO_2 surface is promoted by temperature and possibly also by the non-ideal surface morphology of the films investigated here, where extended terrace edges, kinks, and other defect-related low coordination sites may contribute to a further decrease in the barrier for H_2 dissociation. After the initial dissociation, the Cu^{1+} ions present on the surface greatly facilitate further dissociation. This explains the marked increase in Ce^{3+} concentration during the thermal cycle in H_2 experimentally observed by XPS (Figure 1b). The same mechanism allows us to ascribe the increase in the OH-related signal with temperature (Figure 2b) to the gradually more efficient dissociation of H_2 molecules as the temperature is increased, leading to the formation of surface OH groups upon cooling. Although, in the present work, water formation is not explicitly simulated, our recent results for Ag:CeO_2 suggest that water formation and desorption can explain the observed decrease in O 1s/Pt $4p_{3/2}$ ratio already at mild temperatures (Figure 3). The creation of an O vacancy due to water formation and desorption leaves the two Ce ions involved in H_2 dissociation in the 3+ oxidation state. For this reason, the increase in Ce^{3+} concentration with respect to the initial value during the thermal cycle in hydrogen (Figure 1b) can be partly ascribed to the electrons left on the lattice by oxygen vacancy formation and partly to those left by H_2 dissociation and OH formation during the cooling phase. We note that although, in the present work, it was not possible to reliably determine the Cu oxidation state experimentally, previous work showed that Cu^{1+} species can be stabilized both in the form of dopants in ultrathin ceria films[15] and by depositing Cu atoms at RT on a pure ceria surface.[30,49]

Interestingly, the Cu:CeO_2 film in a H_2 environment investigated in this work showed a behavior different from that of both pure CeO_2 and Ag-modified CeO_2 films of the same thickness grown with the same method in the same conditions, although with a higher dopant concentration.[1] A direct comparison of the Ce^{3+} concentration and OH surface concentration with the thermal treatment in H_2 for the Ag- and Cu-doped samples is reported in Figure 6. In the Ag-doped sample, the Ce^{3+} and OH concentrations only show a mild increase upon thermal treatment in H_2, in spite of the higher Ag concentration. Figure 7 summarizes the reactions that are predicted by the model to occur on the two stable doped surfaces, i.e., the surfaces on which the spontaneous formation of the compensating oxygen vacancy has taken place. The scheme shows that on Ag:CeO_2, the formation of an additional O vacancy, or the dissociative absorption of hydrogen, leads to the localization of one of the two electrons on the Ag dopant, which changes its oxidation state from 2+ to 1+, while only one of the electrons is localized on a Ce ion, which changes its

https://doi.org/10.1021/acs.jpcc.2c04442
J. Phys. Chem. C 2022, 126, 18652−18660

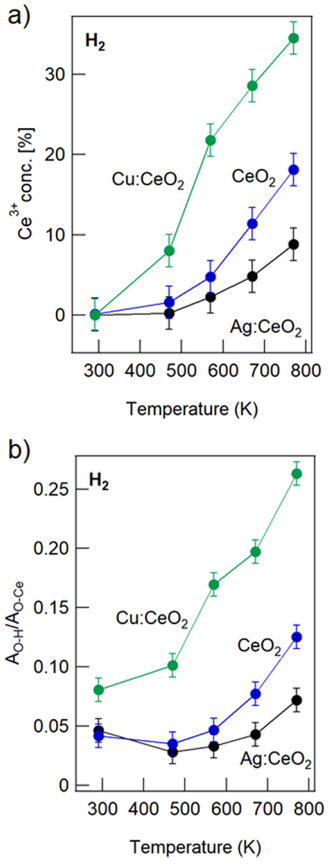

Figure 6. (a) Ce^{3+} concentration and (b) OH surface concentration after the different thermal annealing steps in H_2 for the 3% Cu-doped sample investigated here, a 10% Ag-doped film, and a pure CeO_2 film, with the latter two investigated in ref 1.

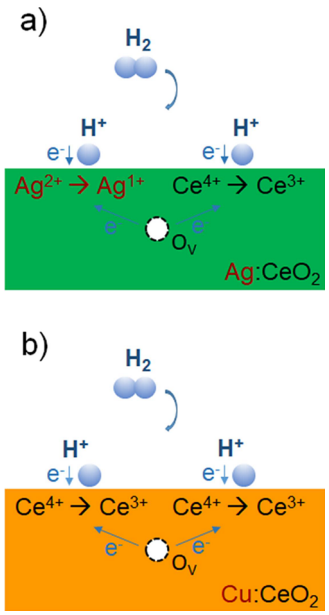

Figure 7. Sketch of the two doped surfaces exposed to H_2 with an O vacancy. (a) On the $Ag:CeO_2$ surface, the dissociative absorption of H_2 or the formation of an O vacancy reduces a Ag atom, which changes its oxidation state from 2+ to 1+, and a Ce atom from 4+ to 3+. (b) On the $Cu:CeO_2$ surface, the dissociative absorption of H_2 or the formation of an O vacancy preferentially reduces two Ce atoms.

formal oxidation state from 4+ to 3+. On the Cu-doped sample, instead, the lower reducibility of Cu as compared to Ag ions makes it much more likely for both electrons left by an O vacancy to localize on two Ce ions. Moreover, the formation energy of the second oxygen vacancy is higher for the Cu-doped sample than for the Ag-doped sample. Therefore, the different redistribution of charge after O vacancy formation or H_2 dissociation in the two systems can explain the more pronounced increase of Ce^{3+} in $Cu:CeO_2$. The rationale for the higher OH surface concentration in the case of the Cu-doped sample with respect to the Ag-doped one during the reduction cycles in hydrogen can be found in the lower concentration of surface O vacancies.

We note that the Ce^{3+} concentration shows a similar trend also in UHV, with the Cu (Ag)-doped sample having a systematically higher (lower) concentration than the undoped film (Figure S6). Moreover, the films investigated here have a significantly lower reducibility in UHV than the much thinner $Cu:CeO_2$ films investigated in ref 15, in agreement with the already observed dependence of the reducibility on the thickness of the film, ascribed to the interaction with the substrate.[50,51]

Ag and Cu dopants exhibit a very different behavior. Ag captures part of the excess electrons released by the oxygen vacancies or when H_2 is dissociatively adsorbed on the surface because Ag^{1+} is the most stable oxidation state. On the contrary, in the case of Cu-doped ceria, the excess electrons prefer to localize on the Ce ions, and Cu keeps its most stable 2+ oxidation state. Interestingly, however, when some Cu^{1+} species are formed, driven by the thermal treatments, the barrier for H_2 dissociation can be significantly decreased, leading to a further increase in the concentration of Ce^{3+} and surface OH groups as compared to the case of pure ceria.

CONCLUSIONS

The surface of a Cu-modified cerium oxide film undergoes important changes with reducing thermal cycles in hydrogen. Although the morphology on a scale of tens of nm is not modified and in spite of the relatively low concentration of Cu atoms within the oxide matrix, a substantial Ce^{3+} concentration is induced by reduction in a hydrogen atmosphere. This is ascribed to the dissociation of H_2, to the associated formation of surface OH groups, and to the creation of O vacancies upon water formation and desorption. DFT modeling has allowed us to attribute the observed changes to the significantly lower barrier for hydrogen dissociation in comparison to pure CeO_2, induced by the presence of highly reactive Cu^{+1} species on the surface. Our results prove that Cu can be a very effective dopant for CeO_2, since it can promote efficient H_2 dissociation at relatively low concentrations.

ASSOCIATED CONTENT

Supporting Information

The Supporting Information is available free of charge at https://pubs.acs.org/doi/10.1021/acs.jpcc.2c04442.

Procedure for the evaluation of Ce^{3+} concentration from the Ce 3d XPS spectra and parameters obtained from the fit; procedure for the fitting of the O 1s XPS spectra and parameters obtained from the fit; procedure for the evaluation of the Cu concentration from the Cu 2p XPS spectra; LEED patterns; STM images after the reducing

https://doi.org/10.1021/acs.jpcc.2c04442
J. Phys. Chem. C 2022, 126, 18652−18660

cycle; comparison of Ce^{3+} concentrations for pure, Ag-doped, and Cu-doped CeO_2 films in UHV (PDF)

AUTHOR INFORMATION

Corresponding Author

Paola Luches − *Institute Nanoscience, National Research Council, Modena 41125, Italy;* orcid.org/0000-0003-1310-5357; Email: paola.luches@nano.cnr.it

Authors

Avinash Vikatakavi − *Department of Physics, Informatics, and Mathematics, University of Modena and Reggio Emilia, Modena 41125, Italy; Institute Nanoscience, National Research Council, Modena 41125, Italy*

Stefania Benedetti − *Institute Nanoscience, National Research Council, Modena 41125, Italy;* orcid.org/0000-0002-2683-4818

Giulia Righi − *Department of Physics, Informatics, and Mathematics, University of Modena and Reggio Emilia, Modena 41125, Italy; Institute Nanoscience, National Research Council, Modena 41125, Italy*

Rita Magri − *Department of Physics, Informatics, and Mathematics, University of Modena and Reggio Emilia, Modena 41125, Italy; Institute Nanoscience, National Research Council, Modena 41125, Italy*

Sergio D'Addato − *Department of Physics, Informatics, and Mathematics, University of Modena and Reggio Emilia, Modena 41125, Italy; Institute Nanoscience, National Research Council, Modena 41125, Italy*

Annabella Selloni − *Department of Chemistry, Princeton University, Princeton, New Jersey 08540, United States;* orcid.org/0000-0001-5896-3158

Complete contact information is available at: https://pubs.acs.org/10.1021/acs.jpcc.2c04442

Notes

The authors declare no competing financial interest.

ACKNOWLEDGMENTS

This work was done with the support of Regione Emilia Romagna POR-FES 2014-2020 project Alte Competenze per la ricerca, il trasferimento tecnologico e l'imprenditorialità "Innovative Materials for fuel cells".

REFERENCES

(1) Benedetti, S.; Righi, G.; Luches, P.; D'Addato, S.; Magri, R.; Selloni, A. Surface Reactivity of Ag-Modified Ceria to Hydrogen: A Combined Experimental and Theoretical Investigation. *ACS Appl. Mater. Interfaces* **2020**, *12*, 27682−27690.

(2) Suryanto, B. H. R.; Wang, Y.; Hocking, R. K.; Adamson, W.; Zhao, C. Overall Electrochemical Splitting of Water at the Heterogeneous Interface of Nickel and Iron Oxide. *Nat. Commun.* **2019**, *10*, 5599.

(3) Graciani, J.; Mudiyanselage, K.; Xu, F.; Baber, A. E.; Evans, J.; Senanayake, S. D.; Stacchiola, D. J.; Liu, P.; Hrbek, J.; Sanz, J. F.; et al. Highly Active Copper-ceria and Copper-ceria-titania Catalysts for Methanol Synthesis from CO_2. *Science* **2014**, *345*, 546.

(4) Lykhach, Y.; Bruix, A.; Fabris, S.; Potin, V.; Matolínová, I.; Matolín, V.; Libuda, J.; Neyman, K. M. Oxide-based Nanomaterials for Fuel Cell Catalysis: the Interplay Between Supported Single Pt Atoms and Particles. *Catal. Sci. Technol.* **2017**, *7*, 4315−4345.

(5) Teschner, D.; Borsodi, J.; Wootsch, A.; Révay, Z.; Hävecker, M.; Knop-Gericke, A.; Jackson, S. D.; Schlögl, R. The Roles of Subsurface Carbon and Hydrogen in Palladium-Catalyzed Alkyne Hydrogenation. *Science* **2008**, *320*, 86.

(6) Mukherjee, S.; Ramalingam, B.; Gangopadhyay, S. Hydrogen Spillover at Sub-2 nm Pt Nanoparticles by Electrochemical Hydrogen Loading. *J. Mater. Chem. A* **2014**, *2*, 3954−3960.

(7) Song, Z.; Norouzi Banis, M.; Liu, H.; Zhang, L.; Zhao, Y.; Li, J.; Doyle-Davis, K.; Li, R.; Knights, S.; Ye, S.; Botton, G. A.; He, P.; Sun, X. Ultralow Loading and High-Performing Pt Catalyst for a Polymer Electrolyte Membrane Fuel Cell Anode Achieved by Atomic Layer Deposition. *ACS Catal.* **2019**, *9*, 5365−5374.

(8) Fiala, R.; Figueroba, A.; Bruix, A.; Vaclavu, M.; Rednyk, A.; Khalakhan, I.; Vorokhta, M.; Lavkova, J.; Illas, F.; Potin, V.; et al. High Efficiency of Pt^{2+}- CeO_2 Novel Thin Film Catalyst as Anode for Proton Exchange Membrane Fuel Cells. *Appl. Catal. B* **2016**, *197*, 262−270.

(9) Vilé, G.; Bridier, B.; Wichert, J.; Pérez-Ramírez, J. Ceria in Hydrogenation Catalysis: High Selectivity in the Conversion of Alkynes to Olefins. *Angew. Chem., Int. Ed.* **2012**, *51*, 8620−8623.

(10) Fiala, R.; Vaclavu, M.; Rednyk, A.; Khalakhan, I.; Vorokhta, M.; Lavkova, J.; Potin, V.; Matolinova, I.; Matolin, V. Pt−CeOx Thin Film Catalysts for PEMFC. *Catal. Today* **2015**, *240*, 236−241.

(11) Prins, R. Hydrogen Spillover. Facts and Fiction. *Chem. Rev.* **2012**, *112*, 2714−2738.

(12) Skorodumova, N. V.; Simak, S. I.; Lundqvist, B. I.; Abrikosov, I. A.; Johansson, B. Quantum Origin of the Oxygen Storage Capability of Ceria. *Phys. Rev. Lett.* **2002**, *89*, 166601.

(13) Fu, Q.; Saltsburg, H.; Flytzani-Stephanopoulos, M. Active Nonmetallic Au and Pt Species on Ceria-Based Water-Gas Shift Catalysts. *Science* **2003**, *301*, 935.

(14) McFarland, E. W.; Metiu, H. Catalysis by Doped Oxides. *Chem. Rev.* **2013**, *113*, 4391−4427.

(15) Gasperi, G.; Brugnoli, L.; Pedone, A.; Menziani, M. C.; Valeri, S.; Luches, P. Reducibility of Ag- and Cu-Modified Ultrathin Epitaxial Cerium Oxide Films. *J. Phys. Chem. C* **2019**, *123*, 13702−13711.

(16) Ševčíková, K.; Nehasil, V.; Vorokhta, M.; Haviar, S.; Matolín, V.; Matolínová, I.; Mašek, K.; Píš, I.; Kobayashi, K.; Kobata, M.; Nagata, T.; Matsushita, Y.; Yoshikawa, H. Altering Properties of Cerium Oxide Thin Films by Rh Doping. *Mater. Res. Bull.* **2015**, *67*, 5−13.

(17) Trovarelli, A. Catalytic Properties of Ceria and CeO_2-Containing Materials. *Catal. Rev* **1996**, *38*, 439−520.

(18) Kammert, J.; Moon, J.; Wu, Z. A Review of the Interactions Between Ceria and H2 and the Applications to Selective Hydrogenation of Alkynes. *Chin. J. Catal.* **2020**, *41*, 901−914.

(19) Boaro, M.; Colussi, S.; Trovarelli, A. Ceria-Based Materials in Hydrogenation and Reforming Reactions for CO2 Valorization. *Front.Chem.* **2019**, *7*, 28.

(20) Yao, H. C.; Yao, Y. F. Y. Ceria in Automotive Exhaust Catalysts: I. Oxygen storage. *J. Catal.* **1984**, *86*, 254−265.

(21) De Leitenburg, C.; Trovarelli, A.; Kašpar, J. A Temperature-programmed and Transient Kinetic Study of CO_2 Activation and Methanation over CeO2 Supported Noble Metals. *J. Catal.* **1997**, *166*, 98−107.

(22) Giordano, F.; Trovarelli, A.; de Leitenburg, C.; Giona, M. A Model for the Temperature-Programmed Reduction of Low and High Surface Area Ceria. *J. Catal.* **2000**, *193*, 273−282.

(23) Vilé, G.; Colussi, S.; Krumeich, F.; Trovarelli, A.; Pérez-Ramírez, J. Opposite Face Sensitivity of CeO_2 in Hydrogenation and Oxidation Catalysis. *Angew. Chem., Int. Ed.* **2014**, *53*, 12069−12072.

(24) Fernández-Torre, D.; Carrasco, J.; Ganduglia-Pirovano, M. V.; Pérez, R. Hydrogen Activation, Diffusion, and Clustering on CeO_2(111): A DFT+U Study. *J. Chem. Phys.* **2014**, *141*, 014703.

(25) Negreiros, F. R.; Camellone, M. F.; Fabris, S. Effects of Thermal Fluctuations on the Hydroxylation and Reduction of Ceria Surfaces by Molecular H2. *J. Phys. Chem. C* **2015**, *119*, 21567−21573.

(26) Werner, K.; Weng, X.; Calaza, F.; Sterrer, M.; Kropp, T.; Paier, J.; Sauer, J.; Wilde, M.; Fukutani, K.; Shaikhutdinov, S.; Freund, H.-J. Toward an Understanding of Selective Alkyne Hydrogenation on

Ceria: On the Impact of O Vacancies on H2 Interaction with CeO2(111). *J. Am. Chem. Soc.* **2017**, *139*, 17608−17616.
(27) Lykhach, Y.; Figueroba, A.; Camellone, M. F.; Neitzel, A.; Skala, T.; Negreiros, F. R.; Vorokhta, M.; Tsud, N.; Prince, K. C.; Fabris, S.; et al. Reactivity of Atomically Dispersed Pt^{2+} Species Towards H_2: Model Pt-CeO_2 Fuel Cell Catalyst. *Phys. Chem. Chem. Phys.* **2016**, *18*, 7672−7679.
(28) Chen, B.; Ma, Y.; Ding, L.; Xu, L.; Wu, Z.; Yuan, Q.; Huang, W. Reactivity of Hydroxyls and Water on a CeO2(111) Thin Film Surface: The Role of Oxygen Vacancy. *J. Phys. Chem. C* **2013**, *117*, 5800−5810.
(29) Wang, X.; Rodriguez, J. A.; Hanson, J. C.; Gamarra, D.; Martínez-Arias, A.; Fernández-García, M. Unusual Physical and Chemical Properties of Cu in Ce1-xCuxO2 Oxides. *J. Phys. Chem. B* **2005**, *109*, 19595−19603.
(30) Righi, G.; Magri, R.; Selloni, A. H_2 Dissociation on Noble Metal Single Atom Catalysts Adsorbed on and Doped into CeO_2 (111). *J. Phys. Chem. C* **2019**, *123*, 9875−9883.
(31) Luches, P.; Pagliuca, F.; Valeri, S. Morphology, Stoichiometry, and Interface Structure of CeO_2 Ultrathin Films on Pt(111). *J. Phys. Chem. C* **2011**, *115*, 10718−10726.
(32) Grinter, D. C.; Ithnin, R.; Pang, C. L.; Thornton, G. Defect Structure of Ultrathin Ceria Films on Pt(111): Atomic Views from Scanning Tunnelling Microscopy. *J. Phys. Chem. C* **2010**, *114*, 17036−17041.
(33) Skála, T.; Šutara, F.; Škoda, M.; Prince, K. C.; Matolín, V. Palladium Interaction with CeO 2 Sn−Ce−O and Ga−Ce−O Layers. *J. Phys. Condens. Matter* **2009**, *21*, 055005.
(34) Skála, T.; Šutara, F.; Prince, K. C.; Matolín, V. Cerium Oxide Stoichiometry Aalteration via Sn Deposition: Influence of Temperature. *J. Electron Spectrosc. Relat. Phenom.* **2009**, *169*, 20−25.
(35) Horcas, I.; Fernández, R.; Gómez-Rodríguez, J. M.; Colchero, J.; Gómez-Herrero, J.; Baro, A. M. WSXM: A Software for Scanning Probe Microscopy and a Tool for Nanotechnology. *Rev. Sci. Instrum.* **2007**, *78*, 013705.
(36) Giannozzi, P.; Baroni, S.; Bonini, N.; Calandra, M.; Car, R.; Cavazzoni, C.; Ceresoli, D.; Chiarotti, G. L.; Cococcioni, M.; Dabo, I.; et al. QUANTUM ESPRESSO: a Modular and Open-source Software Project for Quantum Simulations of Materials. *J. Phys. Condens. Matter* **2009**, *21*, 395502.
(37) Giannozzi, P.; Andreussi, O.; Brumme, T.; Bunau, O.; Buongiorno Nardelli, M.; Calandra, M.; Car, R.; Cavazzoni, C.; Ceresoli, D.; Cococcioni, M.; et al. Advanced Capabilities for Materials Modelling with Quantum ESPRESSO. *J. Phys. Condens. Matter* **2017**, *29*, 465901.
(38) Perdew, J. P.; Burke, K.; Ernzerhof, M. Generalized Gradient Approximation Made Simple [Phys. Rev. Lett. 77, 3865 (1996)]. *Phys. Rev. Lett.* **1997**, *78*, 1396.
(39) Cococcioni, M.; de Gironcoli, S. Linear Response Approach to the Calculation of the Effective Interaction Parameters in the LDA+U Method. *Phys. Rev. B* **2005**, *71*, 035105.
(40) Liu, J. Catalysis by Supported Single Metal Atoms. *ACS Catal.* **2017**, *7*, 34−59.
(41) Qiao, B.; Liu, J.; Wang, Y.-G.; Lin, Q.; Liu, X.; Wang, A.; Li, J.; Zhang, T.; Liu, J. Highly Efficient Catalysis of Preferential Oxidation of CO in H2-Rich Stream by Gold Single-Atom Catalysts. *ACS Catal.* **2015**, *5*, 6249−6254.
(42) Henkelman, G.; Uberuaga, B. P.; Jónsson, H. A Climbing Image Nudged Elastic Band Method for Finding Saddle Points and Minimum Energy Paths. *J. Chem. Phys.* **2000**, *113*, 9901−9904.
(43) Bader, R. F. W. Atoms in Molecules. *Encycl. Comput. Chem.* **1998**, 456.
(44) Bosio, N.; Schaefer, A.; Grönbeck, H. Can Oxygen Vacancies in Ceria Surfaces be Measured by O1s Photoemission Spectroscopy? *J. Phys. Condens. Matter* **2022**, *34*, 174004.
(45) Li, Z.; Werner, K.; Qian, K.; You, R.; Płucienik, A.; Jia, A.; Wu, L.; Zhang, L.; Pan, H.; Kuhlenbeck, H.; Shaikhutdinov, S.; Huang, W.; Freund, H.-J. Oxidation of Reduced Ceria by Incorporation of Hydrogen. *Angew. Chem., Int. Ed.* **2019**, *58*, 14686−14693.
(46) Platzman, I.; Brener, R.; Haick, H.; Tannenbaum, R. Oxidation of Polycrystalline Copper Thin Films at Ambient Conditions. *J. Phys. Chem. C* **2008**, *112*, 1101−1108.
(47) Righi, G.; Benedetti, S.; Magri, R. Investigation of the Structural and Electronic Differences Between Silver and Copper Doped Ceria Using the Density Functional Theory. *J. Phys. Condens. Matter* **2022**, *34*, 204010.
(48) Matolín, V.; Matolínová, I.; Dvořák, F.; Johánek, V.; Mysliveček, J.; Prince, K. C.; Skála, T.; Stetsovych, O.; Tsud, N.; Václavů, M.; Šmíd, B. Water Interaction with CeO_2(111)/Cu(111) Model Catalyst Surface. *Catal. Today* **2012**, *181*, 124−132.
(49) Li, G.; Hu, S.; Xu, Q.; Zhu, J. Interaction between Cu Nanoparticles and CeO2(111) Film Surfaces. *J. Phys. Chem. C* **2019**, *123*, 23563−23571.
(50) Luches, P.; Pagliuca, F.; Valeri, S. Structural and Morphological Modifications of Thermally Reduced Cerium Oxide Ultrathin Epitaxial Films on Pt(111). *Phys. Chem. Chem. Phys.* **2014**, *16*, 18848−18857.
(51) Gasperi, G.; Amidani, L.; Benedetti, F.; Boscherini, F.; Glatzel, P.; Valeri, S.; Luches, P. Electronic Properties of Epitaxial Cerium Oxide Films during Controlled Reduction and Oxidation Studied by Resonant Inelastic X-ray Scattering. *Phys. Chem. Chem. Phys.* **2016**, *18*, 20511.

https://doi.org/10.1021/acs.jpcc.2c04442
J. Phys. Chem. C 2022, 126, 18652−18660